INAE Letters (2019) 4:227–239
https://doi.org/10.1007/s41403-019-00082-w

ORIGINAL ARTICLE

Thermophysical Investigation of Unsteady Casson–Carreau Fluid

Emran Khoshrouye Ghiasi[1] · **Reza Saleh**[1]

Received: 15 May 2019 / Accepted: 29 November 2019 / Published online: 6 December 2019

Abstract

In addition to the non-Newtonian fluids (NNFs), thermophysical analysis of NNF–NNF is very useful for developing unsteady flow measurements. This work aims to provide a two dimensional (2-D) optimization problem consisting of thermal radiation, viscous dissipation, and inclined magnetic force based on the Buongiorno mathematical model. In this way, the unsteady 2-D flow is simulated through a permeable shrinking wall, and the governing partial differential equations are reduced to a set of ordinary differential equations which can be easily solved by the robust homotopic approach (RHA). It is shown that the present RHA agrees very well with those numerical and analytical findings available in the open literature. In fact, it can be concluded that employing a desirable solution methodology is essential for nonlinear boundary value problems combined with the thermophysical properties.

Keywords RHA · NNF · Buongiorno mathematical model · Casson type · Carreau type

List of Symbols

n	Power-law index
u, v	Velocity components along x and y axes, respectively ($\mathrm{m\ s^{-1}}$)
g	Gravitational acceleration ($\mathrm{m\ s^{-2}}$)
T	Temperature (K)
T_∞	Ambient temperature
C	Nanoparticle concentration ($\mathrm{kg\ m^{-3}}$)
C_∞	Ambient nanoparticle concentration ($\mathrm{kg\ m^{-3}}$)
B_0	Magnetic field strength ($\mathrm{kg\ s^{-2}\ A^{-1}}$)
c_p	Specific heat at constant pressure ($\mathrm{J\ kg^{-1}\ K^{-1}}$)
k	Thermal conductivity ($\mathrm{W\ m^{-1}\ K^{-1}}$)
q_r	Radiation heat flux ($\mathrm{W\ m^{-2}}$)
D_B	Brownian diffusion coefficient
D_T	Thermophoresis diffusion coefficient
U_w	Velocity at the wall ($\mathrm{m\ s^{-1}}$)
b	Constant ($\mathrm{s^{-1}}$)
a	Parameter correspond to unsteadiness ($\mathrm{s^{-1}}$)
V_w	Mass transfer rate ($\mathrm{m\ s^{-1}}$)
v_0	Suction/blowing parameter (m)
T_w	Wall temperature (K)
T_0	Reference temperature (K)
C_w	Wall nanoparticle concentration ($\mathrm{kg\ m^{-3}}$)
C_0	Reference nanoparticle concentration ($\mathrm{kg\ m^{-3}}$)
a_R	Mean spectral absorption coefficient ($\mathrm{m^2\ kg^{-1}}$)
f	Similarity function
$\bar{a}$	Unsteadiness parameter
Ha	Hartmann number
We	Weissenberg number
Pr	Prandtl number
N_R	Radiation parameter
Nb	Brownian motion parameter
Nt	Thermophoresis parameter
Le	Lewis number
S	Mass suction parameter
C_f	Skin friction coefficient
Nu_x	Local Nusselt number
Sh_x	Local Sherwood number
Re_x	Local Reynolds number

Greek Symbols

τ	Cauchy stress
τ_0	Yield stress
μ	Dynamic viscosity
$\dot{\gamma}$	Shear rate
μ_∞	Infinite shear rate viscosity
μ_0	Zero shear rate viscosity
Γ	Relaxation time
β	Dimensionless parameter which accounts for the transition point between the zero shear rate and power-law regions
υ	Kinematic viscosity

✉ Emran Khoshrouye Ghiasi
khoshrou@yahoo.com

[1] Department of Mechanical Engineering, College of Engineering, Mashhad Branch, Islamic Azad University, Mashhad, Iran

λ Casson fluid parameter
β_T Thermal expansion coefficient
β_C Nanoparticle concentration expansion coefficient
σ Electrical conductivity
ρ Density
α Inclination angle of magnetic field
ε Ratio of effective heat capacity of the nanoparticle to the effective heat capacity of base fluid
σ_{SB} Stefan–Boltzmann constant (W m^{-2} K^{-4})
η Similarity parameter
φ Stream function
θ Non-dimensional temperature
ϕ Non-dimensional nanoparticle concentration
β_1 Thermal buoyancy parameter
β_2 Solute buoyancy parameter

Introduction

The study of immersed bodies surrounded by external flows is crucial for the fluid mechanics. One of the associated concepts for studying the external flows is to utilize the boundary layer theory (BLT). In general, the coupling of BLT with the external flows characterizes the fluid behavior in an adverse pressure gradient (White 2011). It has found many practical applications in engineering industries, for example, to aerodynamics, hydrodynamics, turbulence, transportation, etc. (Sobey 2001). However, there may be one drawback to the BLT which is its failure in the separated flows (Sychev et al. 1998). To remove this limitation, an efficient computational fluid dynamics (CFD) simulation (Versteeg and Malalasekra 2007; Tu et al. 2012; Tannehill et al. 1997; Cebeci 2005; Sengupta 2004; Anderson 1995) was developed. It is worth noting that the CFD simulation is intended not only for the fluid behavior (Besthapu et al. 2017; Deng et al. 2012; Thepsonthi and Özel 2015; Hsiao 2016; Bezi et al. 2018; Mousazadeh et al. 2018; Shit et al. 2017), but also for chemical reactions (Ganapathirao et al. 2015; Ojjela and Kumar 2016; Hussain 2017; Shateyi and Marewo 2018), phase changes (Onyiriuka et al. 2018; Attia et al. 2015; Sheikholeslami and Rokni 2017), multiple flows (Raees et al. 2018; Gorla and Gireesha 2016; Jahan et al. 2018), etc.

Unlike the numerical CFD solutions, some analytic methods do not suffer from long runtime. Furthermore, due to the simplified boundary conditions involved in the CFD simulation (Houghton et al. 2013), an error usually occurs which cannot be neglected. It is noteworthy that although a large variety of analytical methods have been employed to investigate the NBVPs to date (Adesanya et al. 2018; Dehghan et al. 2015; Shahmohamadi and Rashidi 2016; Sayyed et al. 2018; Dib et al. 2015; Mohseni and Rashidi 2017; Khader and Megahed 2014; Lu et al. 2018; Nadeem et al. 2018, 2019), the RHA (Liao 1992, 2003), due to its convergence and effectiveness, can be considered as a powerful tool for discretizing the governing PDEs to an infinite series. In this way, Khoshrouye Ghiasi and Saleh (2018, 2019a, b, c, d) presented homotopic solutions to some problems arising in the BLT with the mixed boundary conditions. They compared and verified their findings with those obtained by the multi-step techniques such as Runge–Kutta and finite difference methods as well. In addition, they indicated that the RHA would be desirable if the NNFs are employed.

Due to the complexity of NNFs through porous media as well as the interaction between the particles (Goldsmith 1999), the RHA has been the centre of attention to date (Hashmi et al. 2017; Mustafa 2017; Abbas et al. 2010; Hayat et al. 2012a, b, 2016, 2017; Shehzad et al. 2018; Imtiaz et al. 2016). Moreover, the yield stress plays a crucial role in characterizing interaction threshold between the particles (Goldsmith 1999). According to rheology's principle (Tanner 2000), accounting for the influence of constitutive law to describe the whole state of NNFs is essential, because the strain generated by the external forces is very large. It is to be noted that regardless of the flow history, the NNFs can be desirable in some processing technologies such as mixing, shear thinning/thickening, surface coating, etc.

As discussed above, although many efforts have been dedicated to investigate the BLT and NNFs simultaneously, there exist a few works concerning the NNF combined with NNF. Here, a brief summary of the most important works undertaken on the thermophysical analysis of NNF–NNF are reviewed. Raju et al. (2017) characterized numerically the magnetohydrodynamic (MHD) response of NNF–NNF over a variable thickness wall. They developed those reported by Khader and Megahed (2013) and showed that the effect of multiple slip can be ignored only in flow regions away from the stretching wall. Gireesha et al. (2017) accounted for the chemical reaction between the three dimensional (3-D) NNF–NNF. They also investigated the volumetric heat release with the magnetic field and nonlinear thermal radiation. They found that the buoyancy-induced flow over a deformable sheet is significantly affected by the mixed convection of NNFs. Kumaran et al. (2018) simulated thermodynamically NNF–NNF along the upwardly concave paraboloid of revolution. They showed that increasing the uniform Lorentz force, which is known as a resistance towards the velocity distribution, causes suppression of the thermal convection. They also found a remarkable agreement with the numerical solutions of heat transfer analysis in alumina–water fluid considering variable thermal conductivity which is reported by Animasaun and Sandeep (2016). Reddy et al. (2017) analyzed peristaltic transport of electrically conducting NNF–NNF through the NDSolve simulation carried out in Mathematica commercial software. They showed that the natural convection buoyancy-induced flow inside in an irregular channel varies with the uneven heating. However, one would expect the pressure loss not to be accelerated if the forced convection is regarded.

In this study, the unsteady Navier–Stokes, energy, and nanoparticle concentration equations are derived to investigate thermophysical characteristics of NNF–NNF over a permeable shrinking wall considering viscous dissipation and inclined magnetic field based on the Buongiorno mathematical model. For this purpose, the governing PDEs are undergone a similarity transformation and then converted to the ODEs. Furthermore, the RHA and its optimization have been employed to obtain the convergent series expressions. The results are compared and validated by those available numerical and analytical findings in the literature. To the best of author's knowledge, no similar work exists to date.

Problem Formulation

Rheological Model

One of the most common NNFs is the Casson type which represents the Cauchy stress via the following constitutive equation (Casson 1959):

$$\tau = \left[\tau_0^{1/n} + (\mu\dot{\gamma})^{1/n}\right]^n, \tag{1}$$

where τ_0 is the yield stress, μ is the dynamic viscosity, $\dot{\gamma}$ is the shear rate, and $n \in \mathbb{Z}$ is the power-law index. It is to be noted that in the case when $n = 1$, the Casson type reduces to an ideal Bingham plastic (Bingham 1922) (see "Appendix 1").

An alternative NNF for describing the less resistance at higher shear rates is the Carreau–Yasuda type which is governed by Tropea et al. (2007):

$$\tau = \mu_\infty + \left(\mu_0 - \mu_\infty\right)\left[1 + (\Gamma\dot{\gamma})^{2\beta}\right]^{(n-1)/2\beta}, \tag{2}$$

where μ_∞ is an infinite shear rate viscosity, μ_0 is the zero shear rate viscosity, Γ is the relaxation time, and $\beta > 0$ is a dimensionless parameter which accounts for the transition point between the zero shear rate and power-law regions. It should be mentioned here that for monomolecular polymers (i.e., $\beta = 1$), Eq. (2) reduces to the generalized Carreau type (Carreau 1972). Furthermore, since $\dot{\gamma} = \sqrt{\frac{1}{2}\left(\dot{\boldsymbol{\gamma}} : \dot{\boldsymbol{\gamma}}\right)}$, and because μ_∞ is assumed to be zero, we have

$$\mu = \mu_0\left[1 + (\Gamma\dot{\gamma})^2\right]^{(n-1)/2}. \tag{3}$$

Governing Equations

Utilizing the Buongiorno mathematical model in which the slip mechanisms between the nanoparticles can be modeled by means of the thermophoresis and Brownian diffusion (Buongiorno 2006), the governing PDEs take the following form:

$$\frac{\partial u}{\partial x} + \frac{\partial v}{\partial y} = 0, \tag{4}$$

$$\begin{aligned}\frac{\partial u}{\partial t} + u\frac{\partial u}{\partial x} + v\frac{\partial u}{\partial y} = \upsilon\left[1 + \frac{1}{\lambda} + \frac{3(n-1)\Gamma^2}{2}\left(\frac{\partial u}{\partial y}\right)^2\right]\frac{\partial^2 u}{\partial y^2} \\ + g\left[\beta_{\mathrm{T}}\left(T - T_\infty\right) + \beta_{\mathrm{C}}\left(C - C_\infty\right)\right] \\ - \frac{\sigma B_0^2}{\rho}u\sin^2\alpha,\end{aligned} \tag{5}$$

$$\begin{aligned}\frac{\partial T}{\partial t} + u\frac{\partial T}{\partial x} + v\frac{\partial T}{\partial y} = \frac{1}{\rho c_{\mathrm{p}}}\left(k\frac{\partial^2 T}{\partial y^2} - \frac{\partial q_{\mathrm{r}}}{\partial y}\right) \\ + \varepsilon\left[D_{\mathrm{B}}\frac{\partial C}{\partial y}\frac{\partial T}{\partial y} + \frac{D_{\mathrm{T}}}{T_\infty}\left(\frac{\partial T}{\partial y}\right)^2\right],\end{aligned} \tag{6}$$

$$\frac{\partial C}{\partial t} + u\frac{\partial C}{\partial x} + v\frac{\partial C}{\partial y} = D_{\mathrm{B}}\frac{\partial^2 C}{\partial y^2} + \frac{D_{\mathrm{T}}}{T_\infty}\frac{\partial^2 T}{\partial y^2}, \tag{7}$$

where υ is the kinematic viscosity, λ is the Casson fluid parameter, g is the gravitational acceleration, β_{T} is the thermal expansion coefficient, T_∞ is the ambient temperature, β_{C} is the nanoparticle concentration expansion coefficient, C_∞ is the ambient nanoparticle concentration, σ is the electrical conductivity, B_0 is the magnetic field strength, ρ is the density, α is the inclination angle of magnetic field, c_{p} is the specific heat at constant pressure, k is the thermal conductivity, q_{r} is the radiation heat flux, $\varepsilon = (\rho c)_{\mathrm{p}}/(\rho c)_{\mathrm{f}}$ is the ratio of effective heat capacity of the nanoparticle to the effective heat capacity of base fluid, D_{B} is the Brownian diffusion coefficient, and D_{T} is the thermophoresis diffusion coefficient.

The associated initial and boundary conditions are given below:

$$\begin{aligned}&u = 0, v = 0, T = T_\infty, C = C_\infty, \quad \text{at} \;\; t = 0, \\ &u = U_{\mathrm{w}}(x,t) = -\frac{bx}{1 - at}, v = V_{\mathrm{w}}(x,t) = \frac{v_0}{(1 - at)^{1/2}}, \\ &T = T_{\mathrm{w}} = T_\infty + \frac{bx^2 T_0 (1 - at)^{-3/2}}{2\upsilon}, \\ &C = C_{\mathrm{w}} = C_\infty + \frac{bx^2 C_0 (1 - at)^{-3/2}}{2\upsilon}, \quad \text{at} \;\; y = 0, \\ &u \to 0, T \to T_\infty, C \to C_\infty, \quad \text{as} \;\; y \to \infty,\end{aligned} \tag{8}$$

where U_{w} is the velocity at the wall, $b > 0$ is a constant with dimension $(\mathrm{time})^{-1}$, a is a parameter corresponds to unsteadiness, V_{w} is the mass transfer rate, v_0 is the suction/blowing parameter, T_{w} is the wall temperature, T_0 is the reference temperature, C_{w} is the wall nanoparticle concentration, and C_0 is the reference nanoparticle concentration.

The Rosseland approximation formula for the radiation heat flux presented in Eq. (6) takes the form (Rosseland 1931):

$$q_{\mathrm{r}} = -\frac{4\sigma_{\mathrm{SB}}}{3a_{\mathrm{R}}}\frac{\partial T^4}{\partial y}, \tag{9}$$

where $\sigma_{\mathrm{SB}} = 5.6697\times 10^{-8}\left[\mathrm{Wm^{-2}\,K^{-4}}\right]$ and a_{R} are the Stefan–Boltzmann constant and mean spectral absorption coefficient, respectively. Assuming that the temperature discrepancy within the flow is very small (Khoshrouye Ghiasi and Saleh 2019c), T^4 can be expanded in Taylor series as

$$T^4 = T_\infty^4 + 4T_\infty^3\left(T - T_\infty\right) + 6T_\infty^2\left(T - T_\infty\right)^2 + \cdots \approx 4T_\infty^3 T - 3T_\infty^4. \tag{10}$$

Upon substitution of Eq. (10) into Eq. (9) and differentiating this with respect to y, Eq. (6) can be rewritten as follows:

$$\begin{aligned}\frac{\partial T}{\partial t} + u\frac{\partial T}{\partial x} + v\frac{\partial T}{\partial y} &= \frac{1}{\rho c_{\mathrm{p}}}\left(k + \frac{16\sigma_{\mathrm{SB}}T_\infty^3}{3a_{\mathrm{R}}}\right)\frac{\partial^2 T}{\partial y^2}\\ &\quad + \varepsilon\left[D_{\mathrm{B}}\frac{\partial C}{\partial y}\frac{\partial T}{\partial y} + \frac{D_{\mathrm{T}}}{T_\infty}\left(\frac{\partial T}{\partial y}\right)^2\right].\end{aligned} \tag{11}$$

Introducing $\eta = y\left(\frac{b}{\upsilon(1-at)}\right)^{1/2}$, $\varphi = x\left(\frac{b\upsilon}{1-at}\right)^{1/2} f(\eta)$, $\theta(\eta) = \frac{T-T_\infty}{T_{\mathrm{w}}-T_\infty}$, and $\phi(\eta) = \frac{C-C_\infty}{C_{\mathrm{w}}-C_\infty}$, the non-dimensional form of governing ODEs is given by

$$\begin{aligned}&\left(1 + \frac{1}{\lambda}\right)\frac{\partial^3 f}{\partial \eta^3} + \left(f - \frac{\bar{a}\eta}{2}\right)\frac{\partial^2 f}{\partial \eta^2}\\ &\quad - \left(\frac{\partial f}{\partial \eta} + \mathrm{Ha}^2\sin^2\alpha + \bar{a}\right)\frac{\partial f}{\partial \eta} + \beta_1\theta + \beta_2\phi\\ &\quad + \frac{3(n-1)}{2}\mathrm{We}\left(\frac{\partial^2 f}{\partial \eta^2}\right)^2\frac{\partial^3 f}{\partial \eta^3} = 0,\\ &\frac{1}{\mathrm{Pr}}\left(1 + \frac{4N_{\mathrm{R}}}{3}\right)\frac{\partial^2\theta}{\partial \eta^2} + \left(f - \frac{\bar{a}\eta}{2} + \mathrm{Nb}\frac{\partial \phi}{\partial \eta}\right)\frac{\partial \theta}{\partial \eta}\\ &\quad + \mathrm{Nt}\left(\frac{\partial \theta}{\partial \eta}\right)^2 = 0,\\ &\frac{\partial^2\phi}{\partial \eta^2} + \mathrm{Le}\left(f - \frac{\bar{a}\eta}{2}\right)\frac{\partial \phi}{\partial \eta} + \frac{\mathrm{Nt}}{\mathrm{Nb}}\frac{\partial^2\theta}{\partial \eta^2} = 0,\end{aligned} \tag{12}$$

where η is the similarity parameter, φ is the stream function, f is the similarity function, θ is the non-dimensional temperature, ϕ is the non-dimensional nanoparticle concentration, $\bar{a} = a/b$ is the unsteadiness parameter, $\mathrm{Ha}^2 = \frac{\sigma B_0^2}{\rho b}$ is the Hartmann number, β_1 is the thermal buoyancy (or mixed convection) parameter, β_2 is the solute buoyancy parameter, $\mathrm{We}^2 = \frac{\Gamma^2 b^3 x^2}{\upsilon(1-at)^3}$ is the Weissenberg number, $\mathrm{Pr} = \frac{\mu c_{\mathrm{p}}}{k}$ is the Prandtl number, $N_{\mathrm{R}} = \frac{4\sigma_{\mathrm{SB}}T_\infty^3}{3a_{\mathrm{R}}k}$ is the radiation parameter, $\mathrm{Nb} = \frac{\varepsilon D_{\mathrm{B}}}{\upsilon}\left(C_{\mathrm{w}} - C_\infty\right)$ is the Brownian motion parameter, $\mathrm{Nt} = \frac{\varepsilon D_{\mathrm{T}}}{\upsilon T_\infty}\left(T_{\mathrm{w}} - T_\infty\right)$ is the thermophoresis parameter, and $\mathrm{Le} = \upsilon/D_{\mathrm{B}}$ is the Lewis number.

The associated boundary conditions are written as

$$\begin{aligned}&f = S, \frac{\partial f}{\partial \eta} = -1, \theta = 1, \phi = 1, \quad \text{at} \quad \eta = 0,\\ &\frac{\partial f}{\partial \eta} \to 0, \theta \to 0, \phi \to 0, \quad \text{as} \quad \eta \to \infty,\end{aligned} \tag{13}$$

where S is the mass suction parameter.

Here, the non-dimensional skin friction coefficient, local Nusselt number, and local Sherwood number are given by

$$C_{\mathrm{f}} = \frac{2\tau_{\mathrm{w}}}{\rho U_{\mathrm{w}}^2}, \mathrm{Nu}_x = \frac{xq_{\mathrm{w}}}{k\left(T_{\mathrm{w}} - T_\infty\right)}, \mathrm{Sh}_x = \frac{xq_{\mathrm{m}}}{D_{\mathrm{B}}\left(C_{\mathrm{w}} - C_\infty\right)}, \tag{14}$$

where

$$\tau_{\mathrm{w}} = \mu\left(1 + \frac{1}{\lambda}\right)\left(\frac{\partial u}{\partial y}\right)_{y=0}, q_{\mathrm{w}} = -k\left(\frac{\partial T}{\partial y}\right)_{y=0}, q_{\mathrm{m}} = -D_{\mathrm{B}}\left(\frac{\partial C}{\partial y}\right)_{y=0}. \tag{15}$$

It is to be noted that substitution of similarity transformations into Eqs. (14) and (15) gives the results:

$$\begin{aligned}&C_{\mathrm{f}}\mathrm{Re}_x^{1/2} = \left(1 + \frac{1}{\lambda}\right)\left(\frac{\partial^2 f}{\partial \eta^2}\right)_{\eta=0}, \mathrm{Nu}_x\mathrm{Re}_x^{-1/2} = -\left(\frac{\partial \theta}{\partial \eta}\right)_{\eta=0},\\ &\mathrm{Sh}_x\mathrm{Re}_x^{-1/2} = -\left(\frac{\partial \phi}{\partial \eta}\right)_{\eta=0},\end{aligned} \tag{16}$$

where $\mathrm{Re}_x = \frac{\rho U_{\mathrm{w}} x}{\mu}$ is the local Reynolds number.

Solution Methodology

Let us consider the initial approximation of f, θ and ϕ as follows:

$$f_0 = S - 1 + e^{-\eta}, \theta_0 = \phi_0 = e^{-\eta}, \tag{17}$$

which must satisfy the boundary conditions given in Eq. (13). According to the definition of homotopy, the auxiliary linear operators can be represented in the form:

$$L_f = \frac{\partial^3 f}{\partial \eta^3} - \frac{\partial f}{\partial \eta}, L_\theta = \frac{\partial^2\theta}{\partial \eta^2} - \theta, L_\phi = \frac{\partial^2\phi}{\partial \eta^2} - \phi, \tag{18}$$

with the properties:

$$\begin{aligned}&L_f\left[C_1 + C_2e^{\eta} + C_3e^{-\eta}\right] = 0, L_\theta = \left[C_4e^{\eta} + C_5e^{-\eta}\right] = 0,\\ &L_\phi\left[C_6e^{\eta} + C_7e^{-\eta}\right] = 0,\end{aligned} \tag{19}$$

where $C_1 - C_7$ are the arbitrary constants. Using $q \in [0, 1]$ as an embedding parameter, the zeroth-order deformation equations are given by

$$
\begin{aligned}
&(1-q)\mathrm{L}_f\left[f(\eta;q)-f_0(\eta)\right]=qh_f\mathrm{N}_f\left[f(\eta;q)\right],\\
&(1-q)\mathrm{L}_\theta\left[\theta(\eta;q)-\theta_0(\eta)\right]=qh_\theta\mathrm{N}_\theta\left[f(\eta;q),\theta(\eta;q),\phi(\eta;q)\right],\\
&(1-q)\mathrm{L}_\phi\left[\phi(\eta;q)-\phi_0(\eta)\right]=qh_\phi\mathrm{N}_\phi\left[f(\eta;q),\theta(\eta;q),\phi(\eta;q)\right],
\end{aligned}
\tag{20}
$$

where h_f, h_θ, and h_ϕ are the nonzero auxiliary parameters, and N_f, N_θ, and N_ϕ are the nonlinear operators which can be expressed as

$$
\begin{aligned}
N_f\left[f(\eta;q)\right]=&\left(1+\frac{1}{\lambda}\right)\frac{\partial^3 f(\eta;q)}{\partial\eta^3}+\left(f(\eta;q)-\frac{\bar{a}\eta}{2}\right)\frac{\partial^2 f(\eta;q)}{\partial\eta^2}-\left(\frac{\partial f(\eta;q)}{\partial\eta}+\mathrm{Ha}^2\sin^2\alpha+\bar{a}\right)\\
&\times\frac{\partial f(\eta;q)}{\partial\eta}+\beta_1\theta(\eta;q)+\beta_2\phi(\eta;q)+\frac{3(n-1)}{2}\mathrm{We}\left(\frac{\partial^2 f(\eta;q)}{\partial\eta^2}\right)^2\frac{\partial^3 f(\eta;q)}{\partial\eta^3},\\
N_\theta\left[f(\eta;q),\theta(\eta;q),\phi(\eta;q)\right]=&\frac{1}{\mathrm{Pr}}\left(1+\frac{4N_{\mathrm{R}}}{3}\right)\frac{\partial^2\theta(\eta;q)}{\partial\eta^2}+\left(f(\eta;q)-\frac{\bar{a}\eta}{2}+\mathrm{Nb}\frac{\partial\phi(\eta;q)}{\partial\eta}\right)\\
&\times\frac{\partial\theta(\eta;q)}{\partial\eta}+\mathrm{Nt}\left(\frac{\partial\theta(\eta;q)}{\partial\eta}\right)^2,\\
N_\phi\left[f(\eta;q),\theta(\eta;q),\phi(\eta;q)\right]=&\frac{\partial^2\phi(\eta;q)}{\partial\eta^2}+\mathrm{Le}\left(f(\eta;q)-\frac{\bar{a}\eta}{2}\right)\frac{\partial\phi(\eta;q)}{\partial\eta}+\frac{\mathrm{Nt}}{\mathrm{Nb}}\frac{\partial^2\theta(\eta;q)}{\partial\eta^2},
\end{aligned}
\tag{21}
$$

with the boundary conditions

$$
\begin{aligned}
&f(\eta;q)=S,\ \frac{\partial f(\eta;q)}{\partial\eta}=-1,\ \theta(\eta;q)=1,\ \phi(\eta;q)=1,\quad \text{at}\ \ \eta=0,\\
&\frac{\partial f(\eta;q)}{\partial\eta}\to 0,\ \theta(\eta;q)\to 0,\ \phi(\eta;q)\to 0,\quad \text{as}\ \ \eta\to\infty.
\end{aligned}
\tag{22}
$$

It is to be noted that as q increases from 0 to 1, $f(\eta;q)$, $\theta(\eta;q)$, and $\phi(\eta;q)$ deform from the initial approximations to the exact solutions. Expanding $f(\eta;q)$, $\theta(\eta;q)$ and $\phi(\eta;q)$ in the Taylor series with respect to q gives

$$
\begin{aligned}
f(\eta;q)&=f_0(\eta)+\sum_{m=1}^{\infty}f_m(\eta)q^m,\\
\theta(\eta;q)&=\theta_0(\eta)+\sum_{m=1}^{\infty}\theta_m(\eta)q^m,\\
\phi(\eta;q)&=\phi_0(\eta)+\sum_{m=1}^{\infty}\phi_m(\eta)q^m,
\end{aligned}
\tag{23}
$$

where

$$
f_m(\eta)=\left(\frac{1}{m!}\frac{\partial^m f(\eta;q)}{\partial q^m}\right)_{q=0},\ \theta_m(\eta)=\left(\frac{1}{m!}\frac{\partial^m\theta(\eta;q)}{\partial q^m}\right)_{q=0},\ \phi_m(\eta)=\left(\frac{1}{m!}\frac{\partial^m\phi(\eta;q)}{\partial q^m}\right)_{q=0}.
\tag{24}
$$

With the proper choice of initial approximations, auxiliary linear operators, and auxiliary parameters, Eq. (23) converges at $q=1$ as

$$
f(\eta)=\sum_{m=0}^{\infty}f_m(\eta),\ \theta(\eta)=\sum_{m=0}^{\infty}\theta_m(\eta),\ \phi(\eta)=\sum_{m=0}^{\infty}\phi_m(\eta).
\tag{25}
$$

Differentiating Eq. (20) m times with respect to q, dividing them by $m!$ and then setting $q=0$, the m th-order deformation equations are constructed as

$$
\begin{aligned}
&L_f\left[f_m(\eta)-\chi_m f_{m-1}(\eta)\right]=h_f R_{f,m}(\eta),\\
&L_\theta\left[\theta_m(\eta)-\chi_m\theta_{m-1}(\eta)\right]=h_\theta R_{\theta,m}(\eta),\\
&L_\phi\left[\phi_m(\eta)-\chi_m\phi_{m-1}(\eta)\right]=h_\phi R_{\phi,m}(\eta),
\end{aligned}
\tag{26}
$$

where

$$
\chi_m=\begin{cases}0, & n\le 1,\\ 1, & n>1,\end{cases}
\tag{27}
$$

$$
\begin{aligned}
R_{f,m}(\eta)=&\left(1+\frac{1}{\lambda}\right)\frac{\partial^3 f_{m-1}}{\partial\eta^3}+\sum_{l=0}^{m-1}f_l\frac{\partial^2 f_{m-l-1}}{\partial\eta^2}-\frac{\bar{a}\eta}{2}\frac{\partial^2 f_{m-1}}{\partial\eta^2}-\sum_{l=0}^{m-1}\frac{\partial f_l}{\partial\eta}\frac{\partial f_{m-l-1}}{\partial\eta}\\
&+\left(\mathrm{Ha}^2\sin^2\alpha+\bar{a}\right)\frac{\partial f_{m-1}}{\partial\eta}+\beta_1\theta_{m-1}+\beta_2\phi_{m-1}+\frac{3(n-1)}{2}\mathrm{We}\sum_{l=0}^{m-1}\left(\sum_{i=0}^{l}\frac{\partial^2 f_{l-i}}{\partial\eta^2}\sum_{j=0}^{i}\frac{\partial^2 f_j}{\partial\eta^2}\frac{\partial^3 f_{i-j}}{\partial\eta^3}\right),\\
R_{\theta,m}(\eta)=&\frac{1}{\mathrm{Pr}}\left(1+\frac{4N_{\mathrm{R}}}{3}\right)\frac{\partial^2\theta_{m-1}}{\partial\eta^2}+\sum_{l=0}^{m-1}f_l\frac{\partial\theta_{m-l-1}}{\partial\eta}-\frac{\bar{a}\eta}{2}\frac{\partial\theta_{m-1}}{\partial\eta}+\mathrm{Nb}\sum_{l=0}^{m-1}\frac{\partial\phi_l}{\partial\eta}\frac{\partial\theta_{m-l-1}}{\partial\eta}+\mathrm{Nt}\sum_{l=0}^{m-1}\frac{\partial\theta_l}{\partial\eta}\frac{\partial\theta_{m-l-1}}{\partial\eta},\\
R_{\phi,m}(\eta)=&\frac{\partial^2\phi_{m-1}}{\partial\eta^2}+\mathrm{Le}\sum_{l=0}^{m-1}f_l\frac{\partial\phi_{m-l-1}}{\partial\eta}-\mathrm{Le}\frac{\bar{a}\eta}{2}\frac{\partial\phi_{m-1}}{\partial\eta}+\frac{\mathrm{Nt}}{\mathrm{Nb}}\frac{\partial^2\theta_{m-1}}{\partial\eta^2},
\end{aligned}
\tag{28}
$$

with the boundary conditions

$$f(\eta) = 0, \frac{\partial f(\eta)}{\partial \eta} = 0, \theta(\eta) = 0, \phi(\eta) = 0, \text{at } \eta = 0, \quad \frac{\partial f(\eta)}{\partial \eta} \to 0, \theta(\eta) \to 0, \phi(\eta) \to 0, \text{as } \eta \to \infty. \tag{29}$$

The general solutions of Eq. (26) in terms of particular solutions (i.e., $f_m^\star(\eta)$, $\theta_m^\star(\eta)$, and $\phi_m^\star(\eta)$) can be written as

$$\begin{aligned} f_m(\eta) &= f_m^\star(\eta) + C_1 + C_2 e^{\eta} + C_3 e^{-\eta}, \\ \theta_m(\eta) &= \theta_m^\star(\eta) + C_4 e^{\eta} + C_5 e^{-\eta}, \\ \phi_m(\eta) &= \phi_m^\star(\eta) + C_6 e^{\eta} + C_7 e^{-\eta}, \end{aligned} \tag{30}$$

where

$$\begin{aligned} C_1 &= -\left(f_m^\star(0) + \frac{\partial f_m^\star(0)}{\partial \eta} \right), C_2 = C_4 = C_6 = 0, \\ C_3 &= \frac{\partial f_m^\star(0)}{\partial \eta}, C_5 = -\theta_m^\star(0), C_7 = -\phi_m^\star(0). \end{aligned} \tag{31}$$

To summarize the above-mentioned RHA, one can serve the following algorithm:

1. Set $m = 1$.
2. Substitute Eq. (17) into Eq. (28) and find $R_{f,1}$, $R_{\theta,1}$ and $R_{\phi,1}$.
3. Substitute $R_{f,1}$, $R_{\theta,1}$, and $R_{\phi,1}$ into Eq. (26).
4. Determine $C_1 - C_7$ and find f_1, θ_1, and ϕ_1.
5. Substitute f_1, θ_1, and ϕ_1 into Eq. (26) and find $R_{f,2}$, $R_{\theta,2}$ and $R_{\phi,2}$.
6. Repeat steps 2–4 m times.
7. Find f_M, θ_M and ϕ_M, where M is the number of iterations.
8. Check for convergence of the series expressions.

One way to accelerate the convergence of RHA is to find the optimal values of auxiliary parameters by minimizing the squared residual errors as follows (Liao 2010):

$$\begin{aligned} \Delta_{f,m} &= \frac{1}{r+1} \sum_{p=0}^{r} \left\{ N_f \left[\sum_{d=0}^{m} f(\eta) \right]_{\eta = p\delta\eta} \right\}^2 \mathrm{d}\eta, \\ \Delta_{\theta,m} &= \frac{1}{r+1} \sum_{p=0}^{r} \left\{ N_\theta \left[\sum_{d=0}^{m} f(\eta), \sum_{d=0}^{m} \theta(\eta), \sum_{d=0}^{m} \phi(\eta) \right]_{\eta = p\delta\eta} \right\}^2 \mathrm{d}\eta, \\ \Delta_{\phi,m} &= \frac{1}{r+1} \sum_{p=0}^{r} \left\{ N_\phi \left[\sum_{d=0}^{m} f(\eta), \sum_{d=0}^{m} \theta(\eta), \sum_{d=0}^{m} \phi(\eta) \right]_{\eta = p\delta\eta} \right\}^2 \mathrm{d}\eta, \end{aligned} \tag{32}$$

where $r = 20$ and $\delta\eta = 0.5$. It is worth noting that the total squared residual error (i.e., $\Delta_{t,m} = \Delta_{f,m} + \Delta_{\theta,m} + \Delta_{\phi,m}$) can be determined by Mathematica package BVPh2.0 (see "Appendix 2").

Results and Discussion

This section is devoted entirely to finding the thermophysical characteristics of unsteady Casson–Carreau fluid over a permeable shrinking wall based on the Buongiorno mathematical model. To this end, the governing physical parameters, unless stated otherwise, are given in Table 1. It is to be noted that after estimating convergence region of the series expressions and comparing the RHA findings with those available in the open literature, an outline of how the governing physical parameters influence the results is also provided.

Convergence Study

Table 2 tabulates the values of auxiliary parameters as well as its associated total squared residual errors at different orders of approximations (i.e., m) with the parameters, as given in Table 1. According to this table, the auxiliary parameters minimize when m is increased for all cases. Furthermore, it follows that the squared residual error achieves the minimum possible value when $h_f = -0.7235$, $h_\theta = -0.9911$, and $h_\phi = -1.0759$ are chosen. Therefore, it can be concluded that the above-mentioned auxiliary parameters are hereafter utilized in this study.

Table 3 investigates the convergence of above-mentioned series expressions through the use of squared residual errors with the parameters, as presented in Table 1. It is seen from this table that the minimum values of squared residual errors can be found at $m = 20$. Under these circumstances, one can expect the convergence of RHA to accelerate as fast as possible.

Table 2 Selection of h_f, h_θ and h_ϕ

	$m = 1$	$m = 2$	$m = 3$	$m = 4$	$m = 5$
h_f	-0.5418	-0.6191	-0.6722	-0.7020	-0.7235
h_θ	-0.8941	-0.9367	-0.9647	-0.9818	-0.9911
h_ϕ	-1.0060	-1.0341	-1.0560	-1.0693	-1.0759
$\Delta_{t,m}$	2.14×10^{-6}	8.37×10^{-7}	3.95×10^{-7}	7.98×10^{-8}	4.63×10^{-8}

Table 1 Governing physical parameters

λ	$\bar{a}$	Ha	α (Khoshrouye Ghiasi and Saleh 2018)	β_1	β_2	n	We	Pr	N_R	Nb	Nt	Le	S
0.4	-0.5	2	45°	-0.1	0.2	3	0.3	6.2	0.1	0.4	0.4	1	2

Table 3 Values of $\Delta_{f,m}$, $\Delta_{\theta,m}$ and $\Delta_{\phi,m}$

m	$\Delta_{f,m}$	$\Delta_{\theta,m}$	$\Delta_{\phi,m}$
2	6.17×10^{-7}	2.04×10^{-7}	1.61×10^{-8}
4	5.90×10^{-8}	1.76×10^{-8}	3.27×10^{-9}
6	6.70×10^{-9}	3.51×10^{-9}	5.86×10^{-10}
8	8.33×10^{-10}	7.73×10^{-10}	9.14×10^{-11}
10	1.01×10^{-10}	6.22×10^{-10}	5.70×10^{-11}
12	4.12×10^{-11}	4.05×10^{-10}	2.69×10^{-11}
14	8.97×10^{-12}	2.24×10^{-10}	8.72×10^{-12}
16	4.36×10^{-12}	9.06×10^{-11}	5.63×10^{-12}
18	9.95×10^{-13}	7.19×10^{-11}	3.03×10^{-12}
20	7.08×10^{-13}	5.56×10^{-11}	1.22×10^{-12}

Comparison and Validation

To verify the effectiveness of the present RHA, Fig. 1 illustrates the variation of skin friction coefficient versus different values of Hartmann number in both $\alpha = 45°$ and $90°$ with $n = 1$, $\mathrm{Pr} = 0.71$, $N_R = 1$, and $\bar{a} = \beta_1 = \beta_2 = \mathrm{We} = \mathrm{Nb} = \mathrm{Nt} = \mathrm{Le} = S = 0$. This figure also represents a comparison between the RHA findings and those reported by Hakeem et al. (2016) obtained through the Runge–Kutta method. It is to be noted here that velocity slip at the boundary reported by Hakeem et al. (2016) is negligibly small.

As it can be observed from Fig. 1, increasing the values of Hartmann number significantly decreases the skin friction coefficient in both cases. Furthermore, the present RHA agrees very well with those numerical findings reported by Hakeem et al. (2016).

Table 4 provides a comparison between the present RHA and those prepared by Bhattacharyya (2011) to show the effect of mass suction parameter in the calculation of skin friction coefficient. The inserted results in this table are given by $\lambda \to \infty$, $n = 1$ and $\bar{a} = \beta_1 = \beta_1 = \mathrm{We} = N_R = \mathrm{Nb} = \mathrm{Nt} = \mathrm{Le} = 0$. Based on the results of Table 4, it is seen that increasing the suction parameter without considering its NNF terms increases the skin friction coefficient. Furthermore, the RHA findings are consistent with those prepared by Bhattacharyya (2011), because the insignificant relative error between them does not exceed 0.0008%.

Table 4 Values of the skin friction coefficient compared with those of Bhattacharyya (2011)

	$S = 2$	$S = 3$	$S = 4$
Present	2.414240	3.302796	4.236101
Bhattacharyya (2011)	2.414217	3.302772	4.236073

According to the results depicted in Table 5, the present RHA is in an excellent agreement with the numerical findings provided by Pal et al. (2014) as well as those of Khan and Pop (2010). It is due to the fact that the present RHA and those reported by Pal et al. (2014) and Khan and Pop (2010) only suffer from a maximum relative error of at most 0.0058% and 0.0141%, respectively. Furthermore, Table 5 shows the variation of heat transfer rate versus different values of Prandtl number with $\lambda \to \infty$, $n = 1$, and $\bar{a} = \mathrm{Ha} = \alpha = \beta_1 = \beta_2 = \mathrm{We} = N_R = \mathrm{Nb} = \mathrm{Nt} = \mathrm{Le} = S = 0.$

It is to be noted here that increasing the values of Prandtl number in Table 2 clearly increases the heat transfer rate. Therefore, in view of Fig. 1 and Tables 4 and 5, one can say that the present RHA, due to its accuracy and short run time, is desirable to have convergent and reliable series expressions.

Parametric Study

Based on the earlier studies (Khoshrouye Ghiasi and Saleh 2018; Zhang et al. 2016; El-Aziz and Afify 2016), the minimum boundary layer thickness would occur for large values

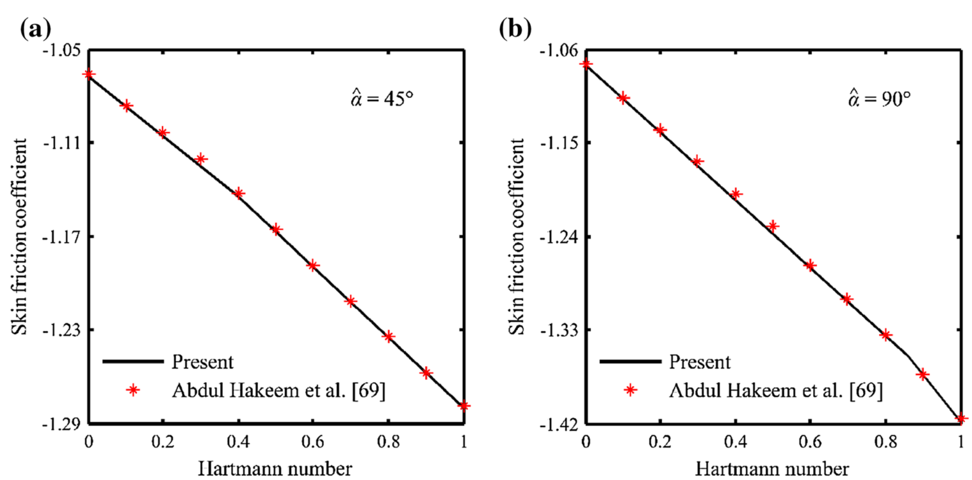

Fig. 1 Verification of the skin friction coefficient for a Casson type; **a** $\alpha = 45°$ and **b** $\alpha = 90°$

Table 5 Values of the heat transfer rate compared with those of Pal et al. (2014) and Khan and Pop (2010)

	Pr = 0.7	Pr = 2	Pr = 7	Pr = 70
Present	0.45398	0.91136	1.89538	6.46218
Pal et al. (2014)	0.45391	0.91135	1.89540	–
Khan and Pop (2010)	0.4539	0.9113	1.8954	6.4621

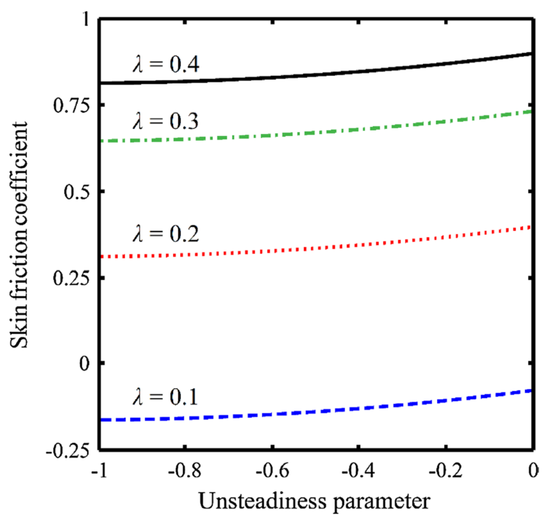

Fig. 2 Variation of $C_f \mathrm{Re}_x^{1/2}$ versus $\bar{a}$

of the unsteadiness parameter. It was shown that this parameter can also be regarded as the induced flow stabilizer. This issue is clearly seen in Fig. 2.

Figure 2 represents the variation of skin friction coefficient versus different values of unsteadiness parameter for $0.1 \le \lambda \le 0.4$. According to this figure, by increasing the Casson fluid parameter, the skin friction coefficient is increased which is only due to a reduction in the diffusion-induced plasticity. However, Mabood et al. (2016) showed that this coefficient becomes relatively insensitive to λ in the case of temperature-dependent dynamic viscosity. It is worth noting that using this observation and the Vogel–Fulcher–Tamman (VFT) law (Vogel 1921), one can modify the temperature dependence of zero shear rate viscosity/relaxation time effectively.

In view of the results given in Table 6, it is seen that the thermal buoyancy parameter plays a more significant role in reducing the skin friction coefficient than that of the solute buoyancy one. This is because of the buoyancy force dominated by the viscous force. Furthermore, the buoyancy effects become more pronounced as the particle and fluid densities are quite different. It is to be mentioned here that a similar conclusion for entropy generation in a heterogeneous porous cavity has also been questioned by Zhuang and Zhu (2018).

Figure 3 depicts the effect of viscoelasticity on the skin friction coefficient for both shear thinning ($n < 1$) and shear thickening ($n > 1$) fluids. Based on the results shown in this figure, increasing the values of Weissenberg parameter decreases the skin friction coefficient which is relevant to the enhancement of the drag force. In addition, since the viscoelasticity depends on the relaxation time, large values of Γ thicken the momentum boundary layer (Khan et al. 2018), and thereby decrease the velocity distribution. Hence, it can be inferred from Fig. 3 that the shear thinning/thickening effect causes little change to the momentum boundary layer thickness.

As shown in Fig. 4, it is obvious that the local Nusselt number is greatly affected by the Brownian motion and thermophoresis parameters simultaneously. Therefore, it is essential to account for the influence of mass diffusivity and temperature gradient with regard to the Brownian motion and thermophoresis parameters, respectively. However, it is to be noted that for large values of Brownian motion parameter, the temperature boundary layer thickness does not significantly vary.

Based on the results presented in Fig. 4, increasing the Browning motion/thermophoresis parameter clearly decreases the local Nusselt number particularly when it is subjected to the shear thickening effect. This is due to the fact that the thermophoresis can be introduced as a time-averaged motion influenced by the Brownian diffusion.

To investigate the effect of thermal radiation on the temperature distribution, the variation of local Nusselt number versus unsteadiness parameter is depicted in Fig. 5. It is seen from this figure that the heat energy which is generated by the radiation process can affect the temperature boundary layer thickness. Furthermore, Fig. 5 emphasizes on the fact that there exists a relationship between the thermal radiation and diffusion in describing the surface heat flux (Khader and Megahed 2014; Nadeem et al. 2019; Farooq et al. 2016).

Table 6 Combined effect of thermal and solute buoyancy parameters on the skin friction coefficient

β_1	$\lambda = 0.5$			$\lambda = 1$		
	$\beta_2 = 0.2$	$\beta_2 = 0.4$	$\beta_2 = 0.6$	$\beta_2 = 0.2$	$\beta_2 = 0.4$	$\beta_2 = 0.6$
−0.1	0.55147	0.53916	0.51701	0.84247	0.81966	0.79990
0	0.51180	0.49266	0.47207	0.78515	0.76117	0.74307
0.1	0.47815	0.45180	0.43014	0.72437	0.70191	0.67899

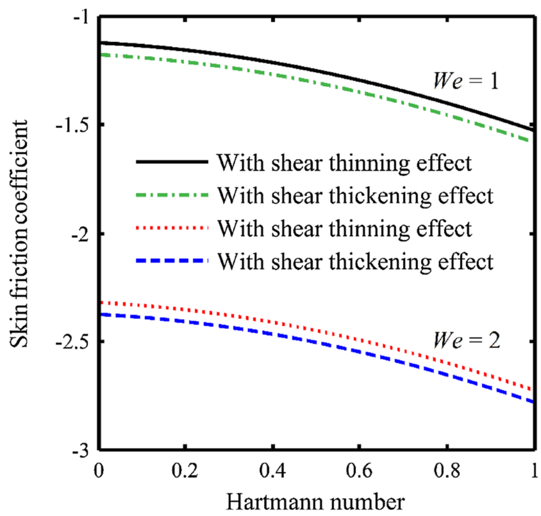

Fig. 3 Variation of $C_f\mathrm{Re}_x^{1/2}$ versus Ha for $n = 0.5$ and 1

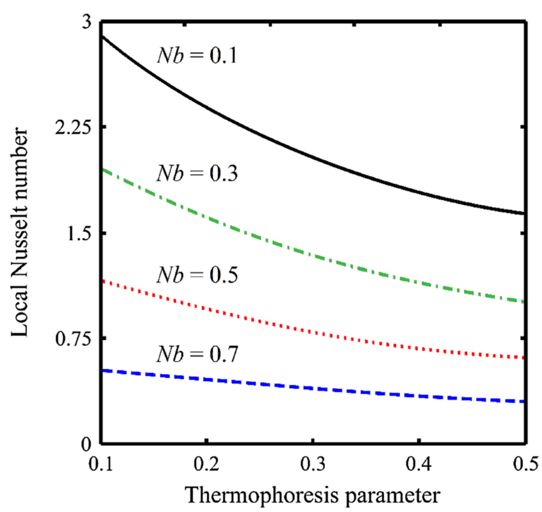

Fig. 4 Variation of $\mathrm{Nu}_x\mathrm{Re}_x^{-1/2}$ versus Nt

Using these important observations, one can conclude that in such systems the thermal radiation cannot be ignored.

Table 7 provides the variation of local Sherwood number versus $\bar{a}$, β_2, Nb, Nt, and Le with both shear thinning and shear thickening fluids. According to this table, by increasing Le, the local Sherwood number is increased which is largely due to a reduction in the Brownian diffusion coefficient. Furthermore, Table 7 represents that the local Sherwood number is an enhancing function of $\bar{a}$, β_2 and Nb, while it is a diminishing function of Nt. At the end of this

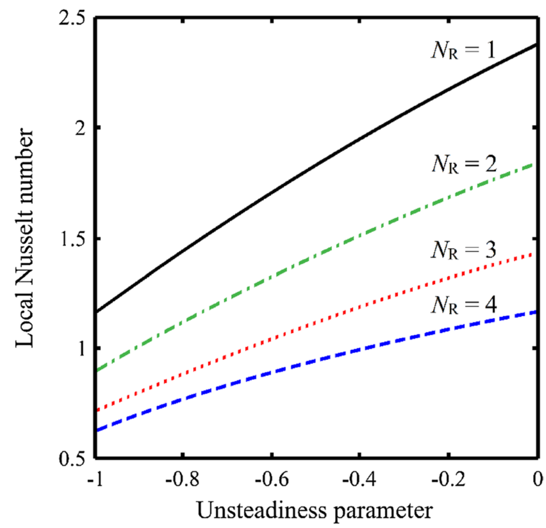

Fig. 5 Variation of $\mathrm{Nu}_x\mathrm{Re}_x^{-1/2}$ versus $\bar{a}$

section, only the velocity, temperature and nanoparticle concentration distributions are listed in Table 8.

Conclusions

The RHA was introduced in this work to investigate thermophysical characteristics of NNF–NNF over a permeable shrinking wall based on the Buongiorno mathematical model. The PDEs that govern the conservation of mass, momentum, energy, and nanoparticle concentration were converted to the ODEs in time via similarity transformation. The present RHA was also optimized by minimizing the squared residual errors at different orders of approximations. Here, the main results of the work can be summarized as follows:

- Accounting for the effect of shear thinning/thickening fluid has little change to its momentum boundary layer thickness.
- In case of $\alpha = 45°$ and 90°, the RHA findings agree excellently with those reported by Hakeem et al. (2016).
- The heat transfer rate is not affected by large values of the Brownian motion parameter. Moreover, the thermophoresis effect cannot be increased without considering the Brownian diffusion.
- The nanoparticle concentration distribution becomes increasingly dependent on the Lewis number.

Table 7 Values of the local Sherwood number

$\bar{a}$	β_2	Nb	Nt	Le	$Sh_x Re_x^{-1/2}$	
					$n = 0.5$	$n = 1.5$
−0.5	0.2	0.4	0.4	1	0.50361	0.72915
−0.4					0.81195	1.07324
−0.3					1.12730	1.29816
−0.3	0.3				1.21919	1.30600
	0.4				1.22746	1.31017
	0.4	0.5			1.53714	1.77195
		0.6			1.91730	1.99899
		0.6	0.5		1.01740	1.10002
			0.6		0.24344	0.27805
			0.6	2	0.86901	0.94629
				3	1.55196	1.74841
				4	2.12302	2.46790

Table 8 Velocity, temperature, and nanoparticle concentration distributions

η	Carreau type			Casson type		
	$\partial f/\partial\eta$	θ	ϕ	$\partial f/\partial\eta$	θ	ϕ
0	−1	1	1	−1	1	1
0.1	−0.9381	0.9519	0.9456	−0.9510	0.9346	0.9768
0.2	−0.9140	0.9160	0.9045	−0.9319	0.8915	0.9528
0.3	−0.8216	0.8826	0.8709	−0.9047	0.8324	0.9479
0.4	−0.7695	0.8524	0.8195	−0.8670	0.7849	0.8930
0.5	−0.7210	0.7938	0.7055	−0.8255	0.7110	0.7915
0.6	−0.6762	0.7244	0.6721	−0.7899	0.6706	0.7065
0.7	−0.6044	0.6531	0.5939	−0.8291	0.6119	0.6206
0.8	−0.5329	0.6030	0.5017	−0.6948	0.5751	0.5937
0.9	−0.5019	0.5207	0.4230	−0.6401	0.4604	0.5417
1	−0.4895	0.4679	0.3573	−0.5973	0.2932	0.4893
2	−0.1836	0.2315	0.0941	−0.3364	0.0914	0.2007
3	−0.1273	0.0195	0.0007	−0.2044	0.0171	0.0715
4	−0.0845	0.0005	0	−0.1178	0.0004	0.0002
5	−0.0316	0	0	−0.0792	0	0
6	−0.0129	0	0	−0.0241	0	0
7	−0.0017	0	0	−0.0114	0	0
8	−0.0008	0	0	−0.0019	0	0
9	0	0	0	−0.0004	0	0
10	0	0	0	0	0	0

Acknowledgements The authors would like to thank the editor and reviewers for their helpful suggestions.

Appendix 1

The constitutive equation for an ideal Bingham plastic which requires a critical force to begin its flow can be written as follows (Bingham 1922):

$$\begin{aligned} &\dot{\gamma} = 0, && \text{for } |\tau| \le |\tau_0|, \\ &\tau = \tau_0 + \mu\dot{\gamma}, && \text{for } |\tau| > |\tau_0|. \end{aligned} \tag{33}$$

As it can be observed from Eq. (33), $\dot{\gamma}$ and τ_0 are usually treated as the curve-fitting constants. It is worth mentioning that although the dynamic viscosity in an ideal Bingham plastic varies linearly, a zero shear rate occurs when the critical force is exceeded (White 2011; Chhabra and Richardson 1999).

Appendix 2

The supplementary data correspond to the Mathematica package BVPh2.0 can be found in the online version at http://numericaltank.sjtu.edu.cn/BVPh.htm.

References

Abbas Z, Wang Y, Hayat T, Oberlack M (2010) Mixed convection in the stagnation-point flow of a Maxwell fluid towards a vertical stretching surface. Nonlinear Anal Real World Appl 11(4):3218–3228. https://doi.org/10.1016/j.nonrwa.2009.11.016

Adesanya SO, Ogunseye HA, Jangili S (2018) Unsteady squeezing flow of a radiative Eyring–Powell fluid channel flow with chemical reactions. Int J Therm Sci 125:440–447. https://doi.org/10.1016/j.ijthermalsci.2017.12.013

Anderson JD (1995) Computational fluid dynamics: the basics with applications. McGraw-Hill, New York

Animasaun IL, Sandeep N (2016) Buoyancy induced model for the flow of 36 nm alumina-water nanofluid along upper horizontal surface of a paraboloid of revolution with variable thermal conductivity and viscosity. Powder Technol 301:858–867. https://doi.org/10.1016/j.powtec.2016.07.023

Attia HA, Abbas W, Abdin AED, Abdeen MAM (2015) Effects of ion slip and Hall current on unsteady Couette flow of a dusty fluid through porous media with heat transfer. High Temp 53(6):891–898. https://doi.org/10.1134/S0018151X15060024

Besthapu P, Haq RU, Bandari S, Al-Mdallal QM (2017) Mixed convection flow of thermally stratified MHD nanofluid over an exponentially stretching surface with viscous dissipation effect. J Taiwan Inst Chem Eng 71:307–314. https://doi.org/10.1016/j.jtice.2016.12.034

Bezi S, Souayeh B, Ben-Cheikh N, Ben-Beya B (2018) Numerical simulation of entropy generation due to unsteady natural convection in a semi-annular enclosure filled with nanofluid. Int J Heat Mass Transf 124:841–859. https://doi.org/10.1016/j.ijheatmasstransfer.2018.03.109

Bhattacharyya K (2011) Effects of radiation and heat source/sink on unsteady MHD boundary layer flow and heat transfer over a shrinking sheet with suction/injection. Front Chem Sci Eng 5(3):376–384. https://doi.org/10.1007/s11705-011-1121-0

Bingham EC (1922) Fluidity and plasticity. McGraw-Hill, New York

Buongiorno J (2006) Convective transport in nanofluids. ASME J Heat Transf 128(3):240–250. https://doi.org/10.1115/1.2150834

Carreau PJ (1972) Rheological equations from molecular network theories. Trans Soc Rheol 16(1):99–128. https://doi.org/10.1122/1.549276

Casson N (1959) Rheology of disperse systems. C.C. Mill, New York

Cebeci T (2005) Computational fluid dynamics for engineers. Springer, New York

Chhabra RP, Richardson JF (1999) Non-Newtonian flow in the process industries. Elsevier Ltd., Oxford

Dehghan M, Rahmani Y, Ganji DD, Saedodin S, Valipour MS, Rashidi S (2015) Convection-radiation heat transfer in solar heat exchangers filled with a porous medium: homotopy perturbation method versus numerical analysis. Renew Energy 74:448–455. https://doi.org/10.1016/j.renene.2014.08.044

Deng SY, Jian YJ, Bi YH, Chang L, Wang HJ, Liu QS (2012) Unsteady electroosmotic flow of power-law fluid in a rectangular microchannel. Mech Res Commun 39(1):9–14. https://doi.org/10.1016/j.mechrescom.2011.09.003

Dib A, Haiahem A, Bou-said B (2015) Approximate analytical solution of squeezing unsteady nanofluid flow. Powder Technol 269:193–199. https://doi.org/10.1016/j.powtec.2014.08.074

El-Aziz MA, Afify AA (2016) Effects of variable thermal conductivity with thermal radiation on MHD flow and heat transfer of Casson liquid film over an unsteady stretching surface. Braz J Phys 46(5):516–525. https://doi.org/10.1007/s13538-016-0442-3

Farooq M, Khan MI, Waqas W, Hayat T, Alsaedi A, Khan MI (2016) MHD stagnation point flow of viscoelastic nanofluid with non-linear radiation effects. J Mol Liq 221:1097–1103. https://doi.org/10.1016/j.molliq.2016.06.077

Ganapathirao M, Ravindran R, Momoniat E (2015) Effects of chemical reaction, heat and mass transfer on an unsteady mixed convection boundary layer flow over a wedge with heat generation/absorption in the presence of suction or injection. Heat Mass Transf 51(2):289–300. https://doi.org/10.1007/s00231-014-1414-1

Gireesha BJ, Kumar PBS, Mahanthesh B, Shehzad SA, Rauf A (2017) Nonlinear 3D flow of Casson–Carreau fluids with homogeneous-heterogeneous reactions: a comparative study. Results Phys 7:2762–2770. https://doi.org/10.1016/j.rinp.2017.07.060

Goldsmith HL (1999) Flow-induced interactions in the circulation. Rheol Ser 8:1–62

Gorla RSR, Gireesha BJ (2016) Dual solutions for stagnation-point flow and convective heat transfer of a Williamson nanofluid past a stretching/shrinking sheet. Heat Mass Transf 52(6):1153–1162. https://doi.org/10.1007/s00231-015-1627-y

Hakeem AKA, Renuka P, Ganesh NV, Kalaivanan R, Ganga B (2016) Influence of inclined Lorentz forces on boundary layer flow of Casson fluid over an impermeable stretching sheet with heat transfer. J Magn Magn Mater 401:354–361. https://doi.org/10.1016/j.jmmm.2015.10.026

Hashmi MS, Khan N, Mahmood T, Shehzad SA (2017) Effect of magnetic field on mixed convection flow of Oldroyd-B nanofluid induced by two infinite isothermal stretching disks. Int J Therm Sci 111:463–474. https://doi.org/10.1016/j.ijthermalsci.2016.09.026

Hayat T, Iqbal Z, Qasim M, Obaidat S (2012a) Steady flow of an Eyring Powell fluid over a moving surface with convective boundary conditions. Int J Heat Mass Transf 55(7–8):1817–1822. https://doi.org/10.1016/j.ijheatmasstransfer.2011.10.046

Hayat T, Iqbal Z, Mustafa M, Alsaedi A (2012b) Momentum and heat transfer of an upper-convected Maxwell fluid over a moving surface with convective boundary conditions. Nucl Eng Des 252:242–247. https://doi.org/10.1016/j.nucengdes.2012.07.012

Hayat T, Waqas W, Shehzad SA, Alsaedi A (2016) Stretched flow of Carreau nanofluid with convective boundary condition. Pramana 86(1):3–17. https://doi.org/10.1007/s12043-015-1137-y

Hayat T, Khan M, Muhammad T, Alsaedi A (2017) A useful model for squeezing flow of nanofluid. J Mol Liq 237:447–454. https://doi.org/10.1016/j.molliq.2017.04.111

Houghton EL, Carpenter PW, Collicott SH, Valentine DT (2013) Aerodynamics for engineering students, 6th edn. Elsevier Ltd., Oxford

Hsiao KL (2016) Stagnation electrical MHD nanofluid mixed convection with slip boundary on a stretching sheet. Appl Therm Eng 98:850–861. https://doi.org/10.1016/j.applthermaleng.2015.12.138

Hussain S (2017) Finite element solution for MHD flow of nanofluids with heat and mass transfer through a porous media with thermal radiation, viscous dissipation and chemical reaction effects. Adv Appl Math Mech 9(4):904–923. https://doi.org/10.4208/aamm.2014.m793

Imtiaz M, Hayat T, Alsaedi A (2016) Mixed convection flow of Casson nanofluid over a stretching cylinder with convective boundary conditions. Adv Powder Technol 27(5):2245–2256. https://doi.org/10.1016/j.apt.2016.08.011

Jahan S, Sakidin H, Nazar R, Pop I (2018) Unsteady flow and heat transfer past a permeable stretching/shrinking sheet in a nanofluid: a revised model with stability and regression analyses. J Mol Liq 261:550–564. https://doi.org/10.1016/j.molliq.2018.04.041

Khader MM, Megahed AM (2013) Numerical solution for boundary layer flow due to a nonlinearly stretching sheet with variable thickness and slip velocity. Eur Phys J Plus 128(9):1–7. https://doi.org/10.1140/epjp/i2013-13100-7

Khader MM, Megahed AM (2014) Differential transformation method for studying flow and heat transfer due to stretching sheet embedded in porous medium with variable thickness, variable thermal conductivity, and thermal radiation. Appl Math Mech Engl Ed 35(11):1387–1400. https://doi.org/10.1007/s10483-014-1870-7

Khan WA, Pop I (2010) Boundary-layer flow of a nanofluid past a stretching sheet. Int J Heat Mass Transf 53(11–12):2477–2483. https://doi.org/10.1016/j.ijheatmasstransfer.2010.01.032

Khan M, Irfan M, Khan WA (2018) Thermophysical properties of unsteady 3D flow of magneto Carreau fluid in the presence of chemical species: a numerical approach. J Braz Soc Mech Sci Eng 40(2):1–15. https://doi.org/10.1007/s40430-018-0964-4

Khoshrouye Ghiasi E, Saleh R (2018) Unsteady shrinking embedded horizontal sheet subjected to inclined Lorentz force and Joule heating, an analytical solution. Results Phys 11:65–71. https://doi.org/10.1016/j.rinp.2018.07.026

Khoshrouye Ghiasi E, Saleh R (2019a) Nonlinear stability and thermomechanical analysis of hydromagnetic Falkner-Skan Casson conjugate fluid flow over an angular-geometric surface based on Buongiorno's model using homotopy analysis method and its extension. Pramana 92(1):1–12. https://doi.org/10.1007/s12043-018-1667-1

Khoshrouye Ghiasi E, Saleh R (2019b) Homotopy analysis method for Sakiadis flow of thixotropic fluid. Eur Phys J Plus 134:1–9. https://doi.org/10.1140/epjp/i2019-12449-9

Khoshrouye Ghiasi E, Saleh R (2019c) A convergence criterion for tangent hyperbolic fluid along a stretching wall subjected to inclined electromagnetic field. SeMA J 76(3):521–531. https://doi.org/10.1007/s40324-019-00190-1

Khoshrouye Ghiasi E, Saleh R (2019d) 2D flow of Casson fluid with non-uniform heat source/sink and Joule heating. Front Heat Mass Transf 12:1–7. https://doi.org/10.5098/hmt.12.4

Kumaran G, Sandeep N, Animasaun IL (2018) Computational modeling of magnetohydrodynamic non-Newtonian fluid flow past a paraboloid of revolution. Alexandria Eng J 57(3):1859–1865. https://doi.org/10.1016/j.aej.2017.03.019

Liao SJ (1992) The proposed homotopy analysis technique for the solution of nonlinear problems. PhD thesis, Shanghai Jiao Tong University

Liao SJ (2003) Beyond perturbation: introduction to the homotopy analysis method. Chapman & Hall/CRC Press, Boca Raton

Liao SJ (2010) An optimal homotopy-analysis approach for strongly nonlinear differential equations. Commun Nonlinear Sci Numer Simul 15(8):2003–2016. https://doi.org/10.1016/j.cnsns.2009.09.002

Lu D, Ramzan M, Ahmad S, Shafee A, Suleman M (2018) Impact of nonlinear thermal radiation and entropy optimization coatings with hybrid nanoliquid flow past a curved stretched surface. Coatings 8(12):1–15. https://doi.org/10.3390/coatings8120430

Mabood F, Abdel-Rahman RG, Lorenzini G (2016) Effect of melting heat transfer and thermal radiation on Casson fluid flow in porous medium over moving surface with magnetohydrodynamics. J Eng Thermophys 25(4):536–547. https://doi.org/10.1134/S1810232816040111

Mohseni MM, Rashidi F (2017) Analysis of axial annular flow for viscoelastic fluid with temperature dependent properties. Int J Therm Sci 120:162–174. https://doi.org/10.1016/j.ijthermalsci.2017.05.025

Mousazadeh SM, Shahmardan MM, Tavangar T, Hosseinzadeh K, Ganji DD (2018) Numerical investigation on convective heat transfer over two heated wall-mounted cubes in tandem and staggered arrangement. Theor Appl Mech Lett 8(3):171–183. https://doi.org/10.1016/j.taml.2018.03.005

Mustafa M (2017) An analytical treatment for MHD mixed convection boundary layer flow of Oldroyd-B fluid utilizing non-Fourier heat flux model. Int J Heat Mass Transf 113:1012–1020. https://doi.org/10.1016/j.ijheatmasstransfer.2017.06.002

Nadeem S, Ahmad S, Muhammad N (2018) Computational study of Falkner–Skan problem for a static and moving wedge. Sens Actuators B Chem 263:69–76. https://doi.org/10.1016/j.snb.2018.02.039

Nadeem S, Khan MN, Muhammad N, Ahmad S (2019) Mathematical analysis of bio-convective micropolar nanofluid. J Comput Des Eng 6(3):233–242. https://doi.org/10.1016/j.jcde.2019.04.001

Ojjela O, Kumar NN (2016) Unsteady MHD mixed convective flow of chemically reacting and radiating couple stress fluid in a porous medium between parallel plates with Soret and Dufour effects. Arab J Sci Eng 41(5):1941–1953. https://doi.org/10.1007/s13369-016-2045-2

Onyiriuka EJ, Obanor AI, Mahdavi M, Ewim DRE (2018) Evaluation of single-phase, discrete, mixture and combined model of discrete and mixture phases in predicting nanofluid heat transfer characteristics for laminar and turbulent flow regimes. Adv Powder Technol 29(11):2644–2657. https://doi.org/10.1016/j.apt.2018.07.013

Pal D, Mandal G, Vajravelu K (2014) Flow and heat transfer of nanofluids at a stagnation point flow over a stretching/shrinking surface in a porous medium with thermal radiation. Appl Math Comput 238:208–224. https://doi.org/10.1016/j.amc.2014.03.145

Raees A, Wang RZ, Xu H (2018) A homogeneous-heterogeneous model for mixed convection in gravity-driven film flow of nanofluids. Int Commun Heat Mass Transf 95:19–24. https://doi.org/10.1016/j.icheatmasstransfer.2018.03.015

Raju CSK, Priyadarshini P, Ibrahim SM (2017) Multiple slip and cross diffusion on MHD Carreau-Cassonfluid over a slendering sheet with non-uniform heat source/sink. Int J Appl Comput Math 3(1):203–224. https://doi.org/10.1007/s40819-017-0351-3

Reddy MG, Prasannakumara BC, Makinde OD (2017) Cross diffusion impacts on hydromagnetic radiative peristaltic Carreau–Casson nanofluids flow in an irregular channel. Defect Diffus Forum 377:62–83. https://doi.org/10.4028/www.scientific.net/DDF.377.62

Rosseland S (1931) Astrophysik und atom-theoretische grundlagen. Springer, Berlin

Sayyed SR, Singh BB, Bano N (2018) Analytical solution of MHD slip flow past a constant wedge within a porous medium using DTM-Padé. Appl Math Comput 321:472–482. https://doi.org/10.1016/j.amc.2017.10.062

Sengupta TP (2004) Fundamentals of computational fluid dynamics. Orient Longman, Hyderabad

Shahmohamadi H, Rashidi MM (2016) VIM solution of squeezing MHD nanofluid flow in a rotating channel with lower stretching porous surface. Adv Powder Technol 27(1):171–178. https://doi.org/10.1016/j.apt.2015.11.014

Shateyi S, Marewo GT (2018) Numerical solution of mixed convection flow of an MHD Jeffery fluid over an exponentially stretching sheet in the presence of thermal radiation and chemical reaction. Open Phys 16(1):249–259. https://doi.org/10.1515/phys-2018-0036

Shehzad SA, Hayat T, Alsaedi A (2018) MHD flow of a Casson fluid with power law heat flux and heat source. Comput Appl Math 37(3):2932–2942. https://doi.org/10.1007/s40314-017-0492-3

Sheikholeslami M, Rokni HB (2017) Effect of melting heat transfer on nanofluid flow in existence of magnetic field considering

Buongiorno model. Chin J Phys 55(4):1115–1126. https://doi.org/10.1016/j.cjph.2017.04.019

Shit GC, Haldar R, Mandal S (2017) Entropy generation on MHD flow and convective heat transfer in a porous medium of exponentially stretching surface saturated by nanofluids. Adv Powder Technol 28(6):1519–1530. https://doi.org/10.1016/j.apt.2017.03.023

Sobey IJ (2001) Introduction to interactive boundary layer theory. Oxford University Press, New York

Sychev VV, Ruban AI, Sychev VV, Korolev GL (1998) Asymptotic theory of separated flows. Cambridge University Press, New York

Tannehill JC, Anderson DA, Pletcher RH (1997) Computational fluid mechanics and heat transfer, 2nd edn. Taylor & Francis, Bristol

Tanner RI (2000) Engineering rheology, 2nd edn. Oxford University Press, New York

Thepsonthi T, Özel T (2015) 3-D finite element process simulation of micro-end milling Ti-6Al-4 V titanium alloy: experimental validations on chip flow and tool wear. J Mater Process Technol 221:128–145. https://doi.org/10.1016/j.jmatprotec.2015.02.019

Tropea C, Yarin A, Foss JF (2007) Springer handbook of experimental fluid mechanics. Springer, Berlin

Tu J, Yeoh GH, Liu C (2012) Computational fluid dynamics: a practical approach, 2nd edn. Elsevier Ltd., Burlington

Versteeg H, Malalasekra W (2007) An introduction to computational fluid dynamics: the finite volume method. Prentice-Hall, Upper Saddle River

Vogel H (1921) Das temperature-abhängigketsgesetz der viskosität von flüssigkeiten. Phys Z 22:645–646

White FM (2011) Fluid mechanics, 7th edn. McGraw-Hill, New York

Zhang Y, Zhang M, Bai Y (2016) Flow and heat transfer of an Oldroyd-B nanofluid thin film over an unsteady stretching sheet. J Mol Liq 220:665–670. https://doi.org/10.1016/j.molliq.2016.04.108

Zhuang YJ, Zhu QY (2018) Analysis of entropy generation in combined buoyancy-Marangoni convection of power-law nanofluids in 3D heterogeneous porous media. Int J Heat Mass Transf 118:686–707. https://doi.org/10.1016/j.ijheatmasstransfer.2017.11.013